


Article

Unveiling Temperature Distribution and Residual Stress Evolution of Additively Manufactured Ti6Al4V Alloy: A Thermomechanical Finite Element Simulation

Qihong Fang ¹, Pei Zhao ^{1,2}, Jia Li ¹ , Hong Wu ³ and Jing Peng ^{1,*}

¹ State Key Laboratory of Advanced Design and Manufacturing for Vehicle Body, College of Mechanical and Vehicle Engineering, Hunan University, Changsha 410082, China; fangqh1327@hnu.edu.cn (Q.F.); nin10284@hnu.edu.cn (P.Z.); lijia123@hnu.edu.cn (J.L.)

² Xi'an Sailong AM Technologies Co., Ltd., Xi'an 710018, China

³ State Key Laboratory of Powder Metallurgy, Central South University, Changsha 410083, China; hwucsu@csu.edu.cn

* Correspondence: jingpeng@hnu.edu.cn

Abstract: The performance of the selective electron beam melting (SEBM) products depends on the SEBM-induced temperature and stress. Here, the thermomechanical finite element simulations are conducted to investigate the dynamic evolution of temperature and the thermal stress of melt pool during the SEBM process of Ti6Al4V alloys under various processing parameters and scanning strategies. The results show that the melt pool undergoes three stages of preheating, melting, and remelting under the influence of adjacent scanning tracks. This complex thermal history drives significant changes in thermal stress within the melt pool. After adjusting the processing parameters, it is found that a low scanning speed and high electron beam energy result in a high temperature gradient and stress in the molten pool. Compared to the electron beam energy, the scanning speed has a more significant impact on temperature and residual stress. For the dual-electron-beam scanning strategy, the coupling thermal effect between electron beams can reduce the temperature gradient of the melt pool, thereby suppressing the formation of columnar crystals. The electron beam energy of 300 W and the scanning speed of 1.5 m/s can be selected under various scanning strategies, which are expected to suppress the formation of coarse and columnar β grains and achieve relatively low residual stress. These results contribute to providing a theoretical basis for selecting optimized process parameters and scanning strategies.

Keywords: selective electron beam melting; finite element models; temperature field; residual stress; scanning strategy



Academic Editor: Giovanni Meneghetti

Received: 20 December 2024

Revised: 14 January 2025

Accepted: 15 January 2025

Published: 17 January 2025

Citation: Fang, Q.; Zhao, P.; Li, J.; Wu, H.; Peng, J. Unveiling Temperature Distribution and Residual Stress Evolution of Additively Manufactured Ti6Al4V Alloy: A Thermomechanical Finite Element Simulation. *Metals* **2025**, *15*, 83. <https://doi.org/10.3390/met15010083>

Copyright: © 2025 by the authors. Licensee MDPI, Basel, Switzerland. This article is an open access article distributed under the terms and conditions of the Creative Commons Attribution (CC BY) license (<https://creativecommons.org/licenses/by/4.0/>).

1. Introduction

Additive manufacturing (AM) technology, which employs the layer-by-layer design strategy to fabricate alloy components, provides the benefits of convenient composition adjustment, flexible structural design, and the conservation of raw materials [1–3]. Thus, it has garnered extensive research and attention in the field of materials manufacturing. Among various AM techniques, selective electron beam melting (SEBM) utilizes a high-energy electron beam as the energy source, demonstrating advantages such as high energy density and high energy absorption efficiency, as well as rapid scanning speeds. These features make it widely applicable in the fabrication of metals with high melting points, high activity, and high brittleness [4,5]. Under the in situ heat treatment effect generated by SEBM preheating, nickel-based alloys exhibit significant gradient structures. The formation

and transformation mechanisms of these structure have been studied [6]. In the dual phase AlCoCuFeNi high-entropy alloy (HEA) prepared by SEBM, the electron beam remelting process results in grain refinement and the formation of phases with a face-centered cubic (FCC) structure, which lead to excellent compressive strength and plasticity in the material [7].

Due to the strong sensitivity of the temperature field inside the melt pool to processing parameters, this affects the microstructure and properties of the material. Ni-based alloys are successfully prepared using SEBM technology, and reasonable processing windows and defect-free criteria are proposed by adjusting the scanning speed and energy density [8]. The significant influence of different scanning speeds on the microstructure and mechanical properties of WMoTaNbTi RHEAs fabricated by SEBM has been revealed, and it has been found that reducing the scanning speed can improve the local plasticity of RHEAs [9]. The density of the alloy fabricated by SEBM is highly sensitive to the electron beam energy. As the energy density increases, the density of Al2024 alloy first increases and then decreases [10]. By optimizing the scanning speed and focal shift during the preparation of 316 L stainless steel using SEBM, the formation of precipitates at grain boundaries is significantly suppressed, leading to improved tensile properties [11].

In addition, the scanning pattern is a key influencing factor on the temperature history, residual stress distribution, and deformation of metals fabricated by AM [12,13]. For example, the scanning strategy significantly affects several characteristics of Ti6Al4V samples, such as relative density, surface morphology, microstructure, and mechanical properties [13]. In the process of multi-channel and multi-layer scanning, a layer-wise inter-lace scan strategy is more conducive to reducing the porosity in the AM product compared to layer-wise rotated scan strategies [14]. An interstitial-strengthened HEA is fabricated by AM with stripe and checkerboard scanning paths, respectively. Under the stripe scanning strategy, it is easier to form an uneven grain morphology and texture, which leads to more severe mechanical anisotropy [15]. In addition, the Laves phase in Ni-based alloy also exhibits the differences in size and distribution under different scanning strategies [16].

Thus, it is crucial to understand the impact of processing parameters and scanning strategies during the AM process before constructing the final structure. The finite element method (FEM) is widely used to reveal the temperature and thermal stress field [17–20]. The temperature field and stress field are obtained under a novel S pattern [17]. The temperature gradient and cooling rate are discussed under several heat source models by the FEM [20]. It is worth noting that, considering the complexity of raw materials and processes, there are numerous factors that affect the performance of AM alloys. It is still difficult to conduct a comprehensive evaluation of these factors.

Ti alloys are widely used for their excellent comprehensive performance [21,22]. In many works, the microstructure-forming and mechanical properties of Ti alloys fabricated by AM have been studied [22,23]. However, the influence of different process parameters and processing strategies of AM technology on the temperature field and thermal stress field of Ti alloys has not been clearly revealed. Thus, in the present work, by considering heat transfer and solid mechanics models, the dynamic evolution of temperature and stress of Ti6Al4V during the SEBM process is revealed, and the effects of different processing parameters and scanning strategies on the thermal and stress history are investigated.

2. Method

2.1. Finite Element Model

In order to investigate the effect of processing parameters and scanning strategies on temperature and stress histories in the Ti6Al4V alloy fabricated by SEBM, a 3D FEM model of single-layer multi-channel electron beam scanning is established using the finite element

software COMSOL 6.2, as shown in Figure 1. The model consists of a substrate with a size of $4\text{ mm} \times 3\text{ mm} \times 0.5\text{ mm}$ and a powder layer with size of $3\text{ mm} \times 2\text{ mm} \times 0.1\text{ mm}$. Considering that the powder size range is about $50\text{--}200\text{ }\mu\text{m}$, with an average size of approximately $100\text{ }\mu\text{m}$ in previous experiments [24,25], the powder layer thickness is set to 0.1 mm here. In order to simplify the model, the powder layer is assumed to be a continuous and uniform metal, and the heat transfer of gas between the gaps in powder is ignored. In addition, the model does not account for the complexity of thermal reactions between the powder alloy and the substrate material during the SEBM process, and it sets the substrate as a Ti6Al4V alloy as well. To ensure calculation accuracy, fine elements with sizes of $25\text{ }\mu\text{m} \times 20\text{ }\mu\text{m} \times 25\text{ }\mu\text{m}$ are adopted in the region of the powder layer. The process parameters are listed in Table 1. The radius of the electron beam is $200\text{ }\mu\text{m}$. The hatch spacing is set to $200\text{ }\mu\text{m}$. According to previous studies, in order to promote the decomposition of the acicular α' martensite phase, a preheating temperature of at least 500 K is required during the preparation of Ti alloy using the powder bed fusion technology [26–28]. Therefore, the substrate and powder layer are set to the preheating temperatures of 500 K and 700 K , respectively. The electron beam energy and scanning speed are selected as processing parameter variables due to them being the main influencing factor [29]. In our model, scanning speeds of 1 m/s , 1.5 m/s and 2 m/s are selected. The electron beam power is 300 W , 400 W , and 500 W , respectively. In addition, according to the difference in the scanning path of the electron beam, the three scanning patterns, including zigzag pattern, raster pattern, and dual-electron beam pattern, are considered, as shown in Figure 2. Furthermore, the thermal conduction model and a solid mechanics model are coupled to simulate the forming process of Ti6Al4V alloy. In the current model, the influence of fluid convection in the melt pool is not taken into account. The influence of material state changes on the temperature and stress inside the melt pool during the melting and solidification process is represented by the variation in material thermal properties with temperature [30]. Detailed explanations are presented in the following sections.

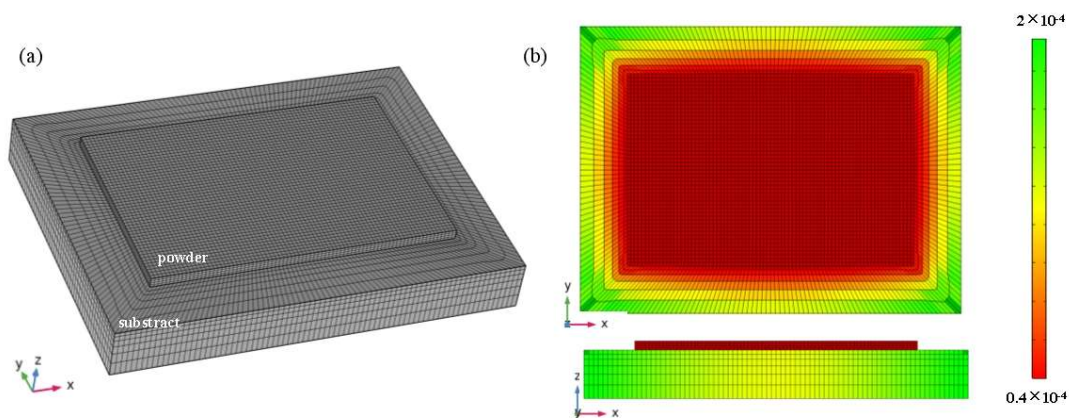


Figure 1. (a) Finite element model of powder bed. (b) Top and side views of the powder bed, colored by element size.

Table 1. The process parameters of SEBM.

Parameter	Value
Heat source power P (W)	300, 400, 500
Scanning speed v (m/s)	1, 1.5, 2
Beam radius R (μm)	200
Preheat temperature T_p (K)	500 for substrate; 700 for powder
Hatch space h_s (μm)	200

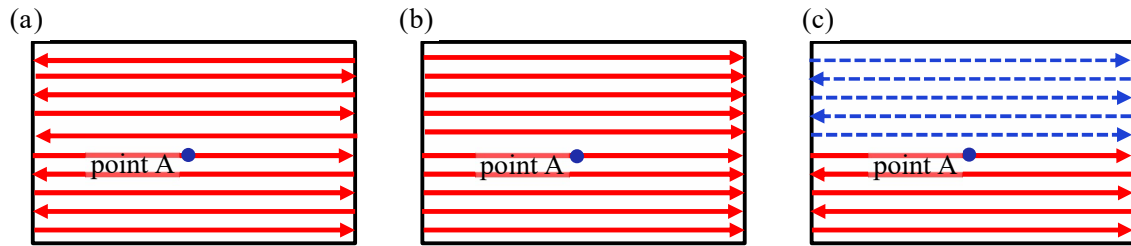


Figure 2. The schematic diagram of scanning pattern: (a) zigzag pattern, (b) raster pattern, (c) dual-electron pattern, where arrows indicate the direction of electron beam scanning. The red and blue arrows represent the paths of the two electron beams, respectively.

2.2. Thermal Model

According to Fourier's law of heat conduction [31], the spatiotemporal distribution of temperature field conforms to the following equation:

$$\frac{\partial}{\partial x} \left(k_x \frac{\partial T}{\partial x} \right) + \frac{\partial}{\partial y} \left(k_y \frac{\partial T}{\partial y} \right) + \frac{\partial}{\partial z} \left(k_z \frac{\partial T}{\partial z} \right) + Q = \rho C \frac{\partial T}{\partial t} \quad (1)$$

where T is the transient temperature distribution of the model, ρ and C are the density and specific heat capacity of the powder material, respectively, t respects the time of heat source action, and k_x , k_y , and k_z are the thermal conductivity of the powder layer in each direction, respectively. Due to the powder layer being assumed to be isotropic, the thermal conductivity can be expressed uniformly as k . Meanwhile, assuming that the powder material is uniformly distributed, the thermal conductivity in all locations is the same. Q is the heat source density. Considering the large penetration depth of electron beam heat sources, the volumetric heat source is adopted [32]. The moving Gaussian distribution heat source [20,33] is widely used, where the energy is maximum at the center of the spot and extends outward while decreasing.

$$Q(x, y, z, t) = 2\varepsilon P I_{xy} I_z \quad (2)$$

where ε is the energy absorption efficiency of the powder material. According to previous studies, compared with the selective melting technology, the energy utilization efficiency is significantly improved during the SEBM process [30]. P is the electron beam energy, I_{xy} represents the energy intensity distribution on the xy plane, and I_z is the energy intensity distribution along the depth direction.

$$I_{xy} = \frac{1}{\pi R^2} \exp \left(-2 \frac{(x - x_s)^2 + (y - y_s)^2}{R^2} \right) \quad (3)$$

where x_s , y_s is the coordinate of the energy center, R is the radius of the electron beam, and z represents the depth coordinates of the energy influence.

The attenuation of energy with depth is expressed as

$$I_z = \frac{1}{\eta} \exp \left(-\frac{|z|}{\eta} \right) \quad (4)$$

where η is the depth of penetration of the electron beam, which is assumed to be the thickness of the powder layer. Before simulating the process of the electron beam scanning, considering the typical process characteristics of SEBM, the substrate and powder layer are preheated to 500 K and 700 K, respectively.

In addition, the heat transfer between the model and the environment is manifested in two forms: convection and radiation of heat between the surface and the environment [19,23].

$$-k \frac{\partial T}{\partial z} \Big|_{z=z_0} = \lambda \zeta (T_{amb}^4 - T^4) + h(T_{amb} - T) \quad (5)$$

Here, only the heat transfer between the top surface of the model with $z = z_0$ and the environment is considered. The first term on the right side of the equation represents the thermal radiation of the powder layer to the environment, and the second term is the thermal convection. λ , ζ , and h are the radiation coefficient, Stephen Boltzmann constant, and heat transfer coefficient, respectively. T_{amb} represents the environment temperature.

2.3. Mechanical Model

In order to obtain the residual stress in the Ti6Al4V alloy fabricated by SEBM, the relationship between the stress and strain in the model is calculated. The material is considered to be an ideal linear elastic material. According to Hooke's law, stress can be expressed as

$$\sigma = \mathbf{C} : \varepsilon^e \quad (6)$$

where σ is the stress tensor, \mathbf{C} is the elastic matrix, and ε^e is the elastic strain tensor. The total deformation of the model includes three parts: elastic deformation, plastic deformation, and thermal deformation [19,34].

$$\varepsilon = \varepsilon^e + \varepsilon^p + \varepsilon^t \quad (7)$$

where ε^p and ε^t represent the plastic strain tensor and the thermal strain tensor. The total strain tensor can be expanded into

$$\begin{cases} \varepsilon_x = \frac{1}{E} [\sigma_x - \nu(\sigma_y + \sigma_z)] + \varepsilon_x^p + \varepsilon^t \\ \varepsilon_y = \frac{1}{E} [\sigma_y - \nu(\sigma_x + \sigma_z)] + \varepsilon_y^p + \varepsilon^t \\ \varepsilon_z = \frac{1}{E} [\sigma_z - \nu(\sigma_x + \sigma_y)] + \varepsilon_z^p + \varepsilon^t \\ \gamma_{xy} = \frac{\tau_{xy}}{2\mu} + \gamma_{xy}^p; \gamma_{yz} = \frac{\tau_{yz}}{2\mu} + \gamma_{yz}^p; \gamma_{xz} = \frac{\tau_{xz}}{2\mu} + \gamma_{xz}^p \end{cases} \quad (8)$$

where E , ν , μ represent the elastic modulus, Poisson's ratio, and shear modulus, respectively. The form of thermal deformation is thermal expansion [19].

$$\varepsilon^t = \alpha_e (T - T_{ref}) \quad (9)$$

where α_e is the coefficient of thermal expansion and T_{ref} is the reference temperature.

The parameters in the thermal and mechanical models are listed in Table 2. The temperature-dependent material parameters are derived from previous research (Figure 3) [23].

Table 2. The parameters of the thermal and mechanical models. Adapted from Refs. [23,35].

Parameter	Value
Elastic modulus E (GPa)	125
Poisson's ration ν	0.34
Material density ρ (Kg/m ³)	443
Energy absorption efficiency ε	0.75

Table 2. Cont.

Parameter	Value
Radiation coefficient λ	0.75
Heat transfer coefficient h	10
Environment temperature T_{amb} (K)	300
Coefficient of thermal expansion α_e	8×10^{-6}
Reference temperature T_{ref} (K)	300

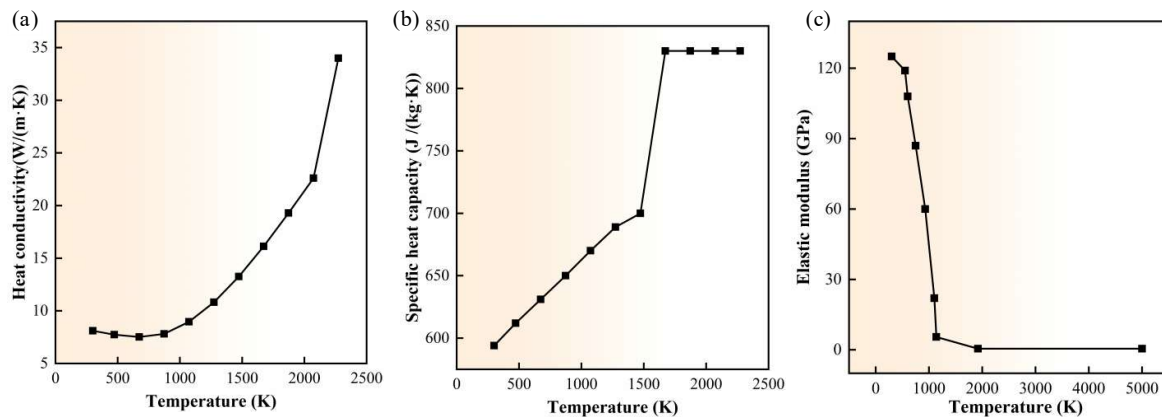


Figure 3. The temperature dependent heat conductivity (a), specific heat capacity (b), and elastic modulus (c). Adapted from Refs. [23,35].

3. Results and Discussion

3.1. Evolution of Melt Pool

Figure 4 compares the temperature curves obtained from experiments and simulations along the scanning track. The experiment used a voltage of 60 KV and a current of 7.2 mA, corresponding to the electron beam power of 432 W in the simulation. The scanning speed is 0.75 m/s. The peak temperature corresponds to the center of the electron beam spot. The simulated peak temperature is about 250 K higher than the experimental peak temperature. This is because the solid pure thermal conduction model used in the present work ignores the influence of fluid convection in the melt pool [36]. Nonetheless, it is evident that the overall trends of the two temperature curves is qualitatively consistent. Both curves show a high temperature gradient near the center of the heat source, and the temperature at the tail of the scanning trajectory is gentle. In addition, the range above the melting point on the temperature curve indicates that the length of the molten pool obtained from both experiments and simulations is approximately the same. The same law is also proven in previous studies [30,36], which further validates the accuracy of the current model.

In order to reveal the temperature field evolution during the multi-channel scanning process, Figure 5a–c exhibit the temperature distribution of the powder bed at a heat source power of 300 W and a scanning speed of 1.5 m/s when the source moves to the fourth, fifth, and sixth track, respectively. The electron beam heat source completes a single-layer and multi-channel scanning process in a zigzag pattern within the powder layer. The blue solid line surrounds the molten pool area where the temperature is higher than the melting point of 1923 K. It can be found that the tail of the molten pool always tills towards the scanned area. The green point A is the midpoint of the fifth track. When the heat source passes through the fourth track, it generates a preheating effect on point A of the neighboring track, which is manifested by the obvious temperature gradient between point A and the substrate. When the heat source scans the fifth track, point A reaches the melting point and

completely melts. As the heat source moves to the sixth track, point A is heated again to near the melting point.

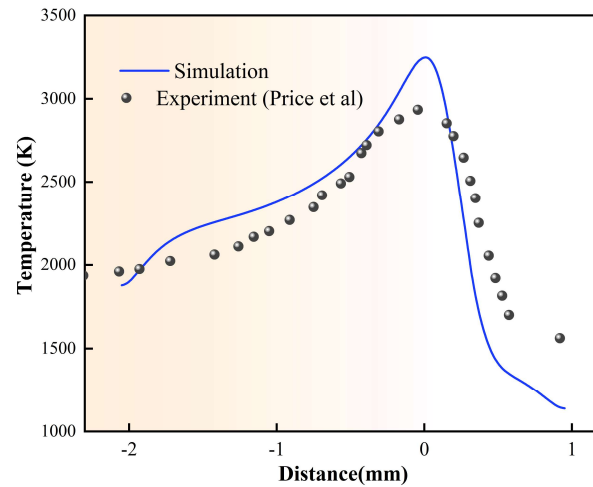


Figure 4. Comparison of simulated temperature curve obtained by the current model and the experimental temperature curve along the scan track. Adapted from Refs. [30,36].

Furthermore, when the heat source moves to point A, the temperature field is analyzed along the scanning direction and perpendicular to it (Figure 6). A long molten pool is presented in Figure 6a. The temperature gradient gradually decreases from the head to the tail of the molten pool. Due to the influence of hatch overlap regions, the temperature field of the current scanning track shows a significant overlap with the temperature field formed by the previous scanning track, which corresponds to the molten pool presented in the experiment (Figure 6b) [37,38]. In addition, changes in the temperature field during the scanning process result in differences in heat transfer efficiency between the scanned and unscanned areas, causing the high-temperature center of the melt pool to deviate from the preset heat source center.

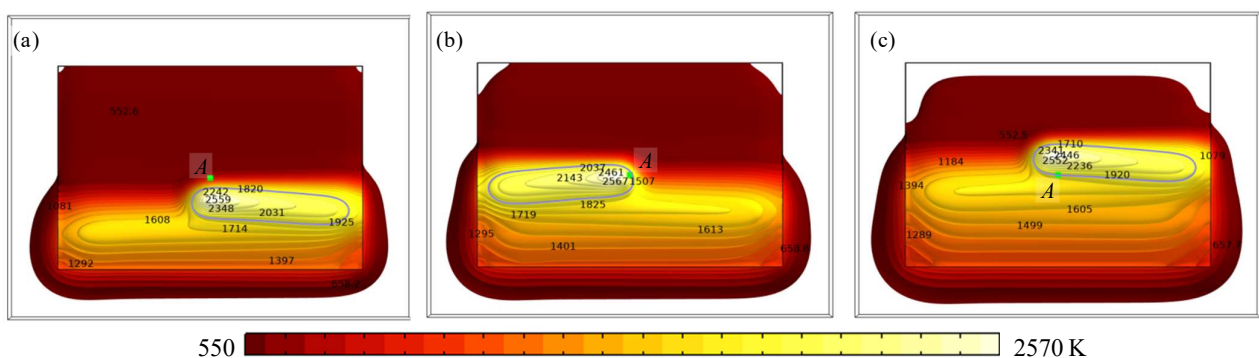


Figure 5. The temperature distribution of the Ti6Al4V alloy powder bed during the scanning process, when the heat source passes through (a) the fourth track, (b) the fifth track, and (c) the sixth track.

3.2. Effect of Processing Parameters

In order to investigate the effects of processing parameters on the formation of Ti6Al4V alloy prepared by SEBM, the temperature and stress history are discussed under different electron beam power and scanning speeds. Similarly, point A, as shown in Figure 2, is selected to output temperature and stress in order to clearly describe the joint impact of the current and adjacent scanning paths on the melt pool. The temperature cycling curves of point A, as depicted in Figure 7, are obtained at a scanning speed of 1.5 m/s and power settings of 300, 400, and 500 W, respectively. As the heat source moves, the temperature

exhibits three distinct stages of increase. It is due to this that the temperature field within the scanning trajectory is affected by the thermal effects of the previous and subsequent scanning electron beams [35]. The selected point A is located on the center-line of fifth track in the current simulation. Initially, as the heat source moves to the fourth track, the temperature at node rises for the first time, exhibiting a brief plateau, which reflects the preheating effect of the previous scanning track on the node. Subsequently, the electron beam heats the fifth track, the temperature rapidly reaches its peak and exceeds the melting point of Ti6Al4V, causing powder melting. The peak temperature of the molten pool is directly proportional to the energy of the heat source and shows a clear linear relationship. That is, as the energy increases by an equal difference, the temperature also exhibits a similar law of equal difference increase. As the electron beam scans to the sixth track, the temperature rises again. Immediately after, the heat source moves to next track without causing an increase in the temperature of the designated node A. Under the effects of thermal diffusion and radiation, the temperature gradually decreases. The cooling rate is crucial for designing a solidification microstructure. The cooling rate is shown in Figure 7b. The high cooling rate characteristic of AM technology is reflected, reaching 10^6 K/s, which is consistent with the previous results [39]. It is evident that the heating rate of the molten pool is significantly higher than that at 300 W when the electron beam power is 500 W. After the temperature of the molten pool reaches its peak, the temperature decreases at a high cooling rate due to the removal of the heat source and heat dissipation. As the energy increases, the cooling rate slightly accelerates.

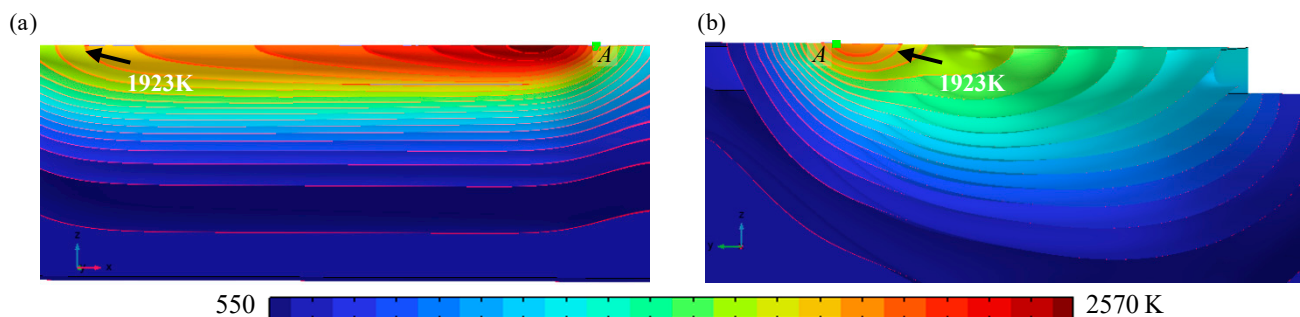


Figure 6. The temperature field of the molten pool (a) along the scanning direction and (b) perpendicular to scanning direction when the heat source moves to point A.

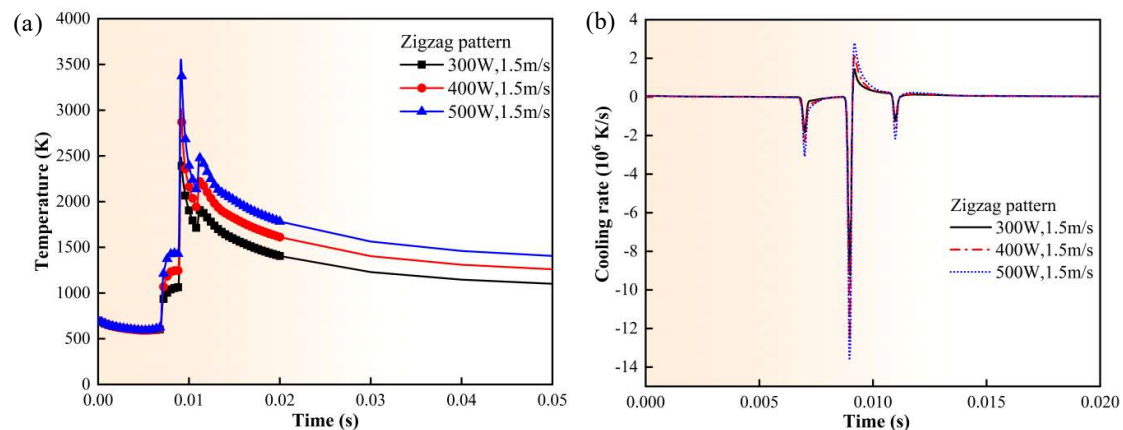


Figure 7. Time-dependent curve of temperature (a) and cooling rate (b) under different electron beam power.

The temperature changes of point A at different scanning speeds of 1 m/s, 1.5 m/s, and 2 m/s, as well as a constant energy of 300 W, are represented in Figure 8. It is clearly visible that node A, located in the fifth track, undergoes three heating processes when the

electron beam scans the fourth, fifth, and sixth tracks [23]. Obviously, as the scanning speed increases, the preheating and remelting temperature generated by adjacent tracks scanned by the heating source at point A decrease.

In addition, as the scanning speed increases, the peak temperature decreases significantly due to the decrease in energy input to the powder layer per unit time. The scanning speed increases at equal intervals, and the temperature change in the melt pool does not exhibit a linear relationship similar to that described in Figure 7a. Thus, the influence of scanning speed on the temperature changes is more remarkable than that of heating source energy [29,40]. The temperature change is more significant when the scanning speed increases from 1.5 m/s to 2 m/s compared to when it increases from 1 m/s to 1.5 m/s. The cooling rate is shown in Figure 8b. The slower the scanning speed, the wider the distance between the heating and cooling rate peaks. A high scanning speed corresponds to a high heating rate and low cooling rate. This phenomenon is completely different from that in Figure 7b for various electron beam power. In addition, compared to changes in energy, changes in scanning speed have a smaller impact on the amplitude of changes in maximum heating rate. In other words, changing the scanning speed has a more significant impact on the temperature of the melt pool compared to changing the input power [41]. In addition, the cooling rate is significantly higher during the solidification stage of the molten pool when the scanning rate is 1 m/s. According to Equation (6), this is attributed to the high heat dissipation effect, which is caused by the significant temperature difference between the melt pool and the environment as well as the increase in thermal conductivity with increasing temperature [23,42]. Considering the relationship between the phase structure and temperature history in AM Ti alloys [43], the β phase is formed in the temperature range of 1923 K to 1268 K. During the further cooling process, the β phase transforms into a finer α phase. As shown in Figures 7a and 8a, when the power reaches 400 W or the scanning speed is below 1 m/s, the higher peak temperature and remelting process result in a longer residence time in the β phase temperature region. Combined with high cooling rates, this may lead to the formation of columnar, coarse β phase regions, resulting in anisotropic behavior in the alloys.

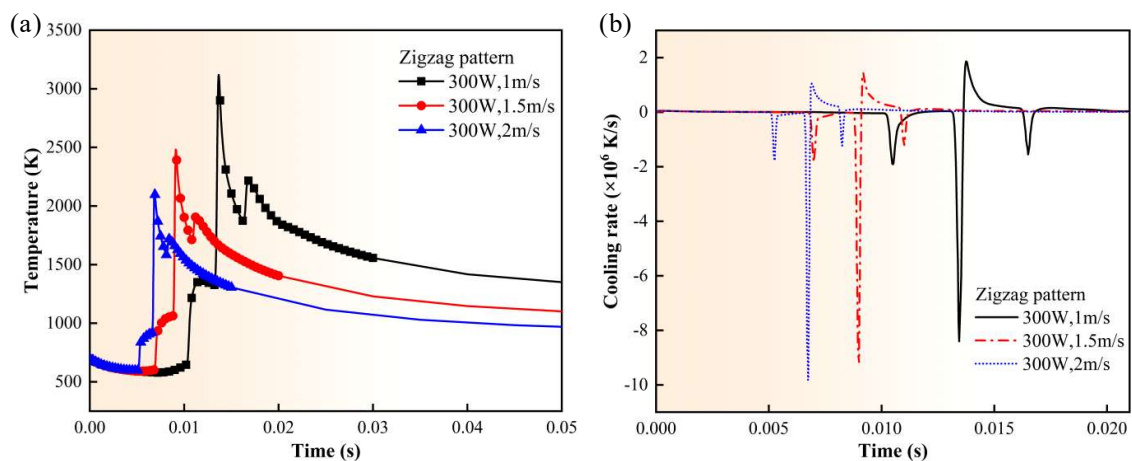


Figure 8. Time-dependent curve of temperature (a) and cooling rate (b) under different scanning speed.

Figure 9 depicts the temperature distribution and molten pool morphology on the top surface under different powers of 300 W, 400 W, and 500 W when the electron beam scans to point A. The solid orange line represents the isotherm at 1923 K, which is the melt point of Ti6Al4V. The enclosed area corresponds to the molten state. During the multi-channel scanning process, due to the inconsistent heat transfer conditions between the

scanned and unscanned areas, the temperature field and molten pool exhibit asymmetric distribution [17,23,42]. The scanned area has a large thermal impact range and a small temperature gradient. Obviously, as the power of the heat source increases, the size of the melt pool and the temperature at the center of the scanning track increases. Figure 10 describes the temperature field under different scanning speeds of 1 m/s, 1.5 m/s, and 2 m/s. Similarly to Figure 8, due to the influence of the adjacent scanning track, the scanned area also exhibits a solidification delay. As the scanning speed increases, the molten area shrinks. When the scanning speed is 2 m/s, the heat-affected zone at the tail of the electron beam shrinks and the melting zone exhibits a conical shape.

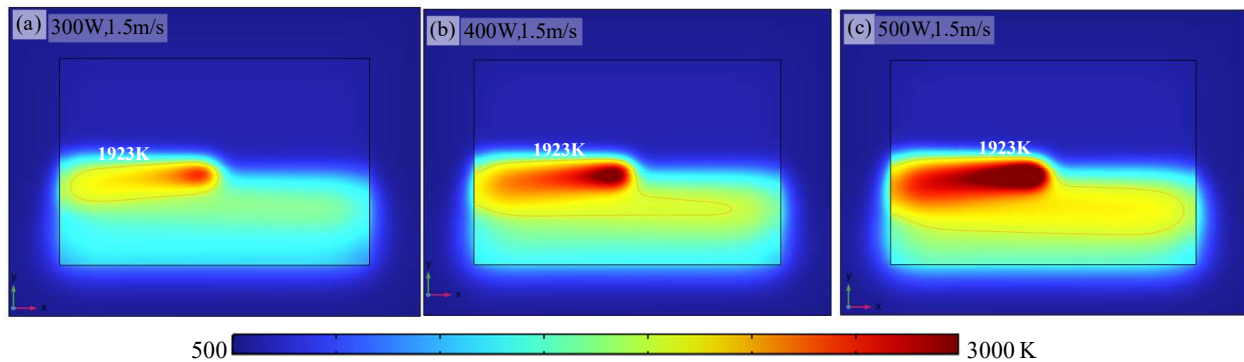


Figure 9. The temperature distribution under different power of (a) 300 W, (b) 400 W, and (c) 500 W for zigzag pattern scanning path.

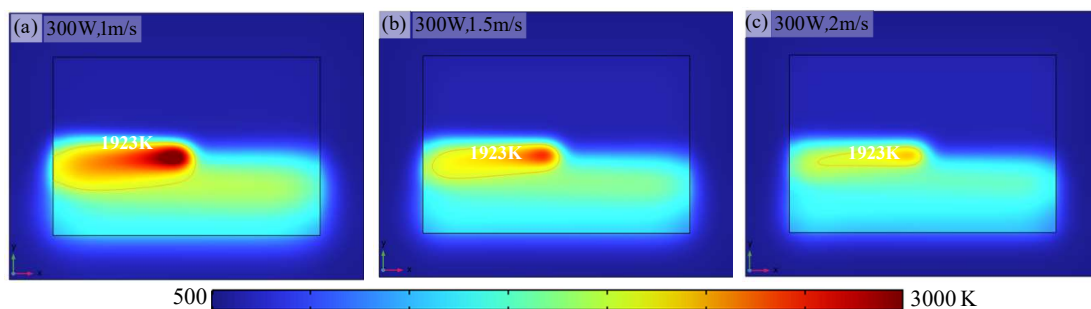


Figure 10. The temperature distribution under different scanning speeds of (a) 1 m/s, (b) 1.5 m/s, and (c) 2 m/s at powder of 300 W for zigzag pattern scanning path.

Furthermore, the stress histories of point A represented by Von mises stress are analyzed under different power and scanning speed as shown in Figure 11. As previously reported, the residual stress of metals fabricated by additive manufacturing is related to the thermal history of melt pool. Thus, the stress evolution is corresponding to the temperature history shown in Figures 7a and 8a. From the curve of stress evolution over time, it can be seen that the stress increases from the molten state to the solidified state, and then gradually decreases during the cooling process. It is worth noting that higher stress values are obtained at low scanning rates or high input power (Figure 11a,c), which is consistent with the previous reports that high energy density increases the thermal shrinkage rate, resulting in high residual stress. This is the fundamental reason for the generation of thermal microcracks inside additive manufacturing components, and also the origin of high density inside alloys [44]. Due to the assumption in our simulation that the powder layer is a continuous and uniform metal layer, there is a high initial stress after preheating. Under the preheat effect generated by scanning the previous track, the elastic modulus of Ti6Al4V alloy decreases (Figure 3c), resulting in a significant decrease in stress. As the heat source passes, the temperature exceeds the melting point and the powder enters a completely melted state, causing the stress to approach 0 MPa. Thus, the attention need to be paid

to the stress changes in the molten pool during the cooling stage after the heat source leaves. The thermal expansion and contraction of the molten pool during the solidification process can affect the microstructure growth state inside the molten pool. In the initial solidification stage, a phase transition from liquid to solid occurs in the molten pool due to the decrease in temperature. At this time, the thermal stress rapidly increases as shown in Figure 11b,d. The changes in scanning speed and power have a significant impact on the thermal stress in the molten pool. As the scanning speed increases, the rate of the thermal stress rise increases. In addition, the increase in power slows down the rate of stress increase. During the subsequent cooling process, thermal stress gradually releases. The thermal stress evolution during solidification leads to thermal shrinkage and expansion deformation, which will affect the grain morphology and dislocation distribution formed in the melt pool [45,46]. According to the previous experimental studies, it was found that the combination of complex thermal history and stress field promotes the generated of high dislocation density, ultimately leading to the formation of dislocation cells [39].

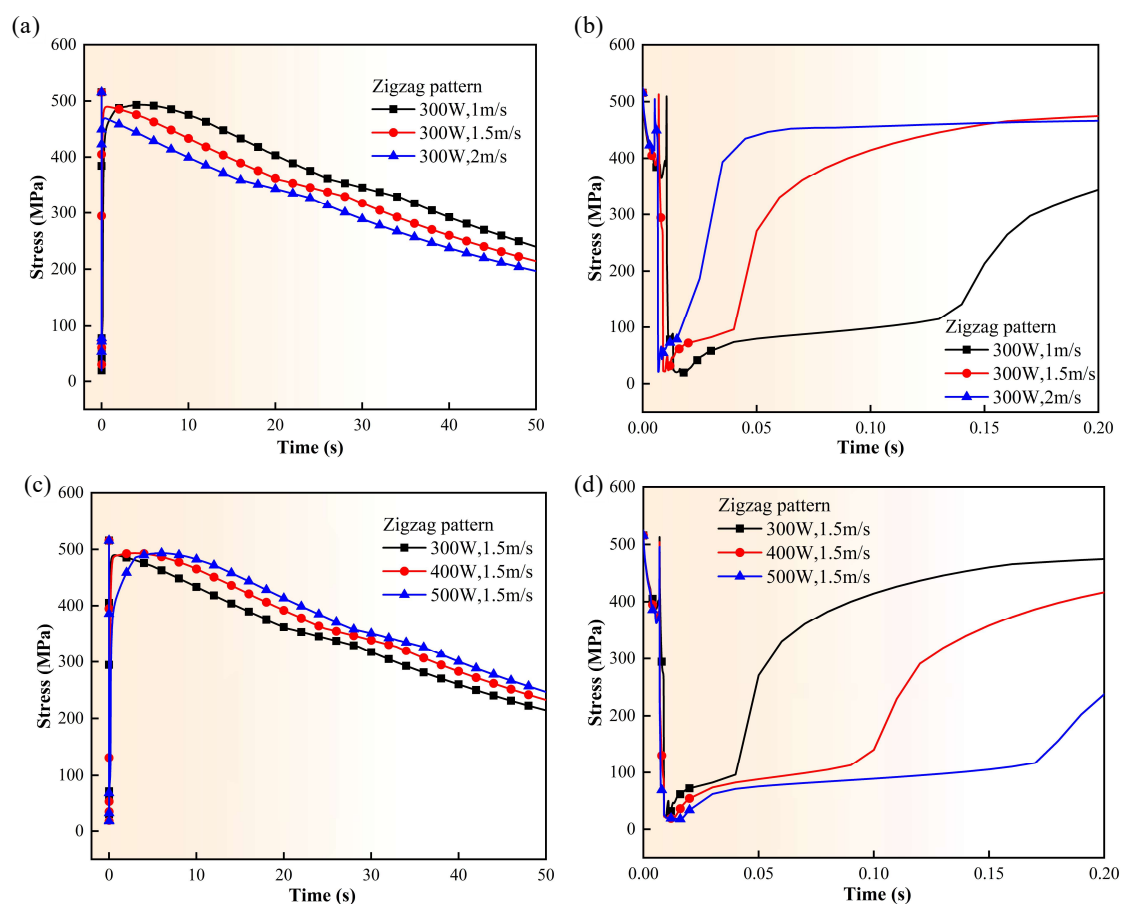


Figure 11. Stress histories under (a,b) different scanning speeds, and (c,d) different power.

3.3. Effect of Scanning Strategy

As is well known, in addition to processing parameters, the scanning strategy also has a significant impact on the temperature, stress field of melting pool, as well as the formation of microstructure. In this section, the scanning path of single electron beam in raster pattern is simulated to compare and analyze the effects of zigzag pattern and raster pattern. Meanwhile, the influence of the dual-electron beam scanning strategy on thermal and stress history is investigated.

3.3.1. Effect of Scanning Path

In order to investigate the effect of the scanning path on temperature and stress history, single-layer and multi-channel scanning processes in a raster pattern within the powder layer are completed at the power of 300 W and various scanning speeds of 1 m/s, 1.5 m/s and 2 m/s. Figure 12 presents the temperature distribution and molten pool morphology on the top surface. As the scanning speed increases, the melting zone shrinks at current moment.

However, the melting zone enclosed by the orange solid line in scanning strategy of raster pattern (Figure 12) are significantly different from that obtained from the zigzag pattern scanning path (Figure 10). Due to the discontinuity of the electron beam scanning path between the fourth track and the fifth track where point A is located, two separate melting region appear at low scanning speed of 1 m/s. In addition, the unidirectional movement mode of the electron beam causes the width of the molten pool to increase from left to right, with clear directionality, which could cause warpage in the formed sample [47]. In contrast, due to the bidirectional movement mode of the electron beam of zigzag pattern, the present track has the potential to compensate for the influence of the previous track. The length of molten pool of raster pattern is smaller than that in zigzag pattern. Thus, the state of the molten pool is greatly affected by the scanning path. The temperature field obtained from the zigzag pattern is more stable than that obtained from the raster pattern. In addition, the temperature and stress histories of point A are exhibited in the Figure 13. The temperature and stress history of point A are almost unaffected under two different scanning strategies [17,47,48]. From the temperature curves of the point A (Figures 8a and 13a), it can be seen that the peak temperature experienced by the melt pool is same in both scanning pattern. Thus, compared with the zigzag pattern, the short molten pool presented in raster pattern means a larger temperature gradient. Combining a longer temperature range for forming the β phase at low scanning speeds makes it easier to promote the formation of coarse and columnar β grains [39]. It is not conducive to the strengthen of AM alloys. In addition, according to the heat transfer and solid mechanics models, thermal stress is mainly affected by the thermal expansion deformation of the melt pool and the elastic constant, which are mainly related to temperature. Therefore, the two scanning modes exhibit almost the same stress conditions under the same temperature history.

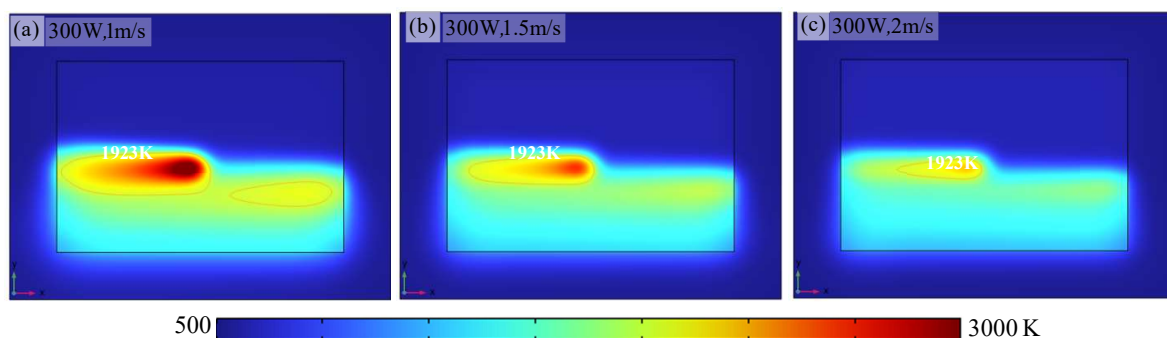


Figure 12. The temperature distribution under different scanning speeds of (a) 1 m/s, (b) 1.5 m/s, and (c) 2 m/s at powder of 300 W for raster pattern scanning path.

3.3.2. Effect of Dual-Electron Beam

The multi-laser powder bed fusion technology has been proven to significantly improve the forming size and efficiency. Similarly, the scanning path with multi-electron beam pattern has the potential to efficiency fabricate large-scale structures [23,49]. However, the multi-electron beam powder bed fusion technology has not yet been fully developed. In this section, the influence of different spatial and temporal effects generated by dual-electron

beam on melting pool is analyzed. The movement paths of two sets of electron beam are shown in Figure 2c. The temperature distribution is exhibited in Figure 14. There are two melting region generated by dual-electron beam. By comparing the upper and lower electron beam scanning areas, the lower electron beam scanning area is affected by the heat of the scanned area of the upper electron beam, resulting in an increase in the length of the melting zone. In addition, compared to the zigzag and raster pattern, the width and the melt pool increases and temperature gradient is smaller for the dual-electron beam pattern, which can be attributed to the preheat effect of the powder when the upper electron beam passes through [50]. Temperature gradient is one of crucial thermodynamic factor on microstructure forming during the process of AM [51–53]. According to the theory of the constitutional undercooling and solidification, the formation of grain morphology is mainly controlled by the temperature gradient (G) and the average growth rate (R). A high G/R ratio promotes the formation of columnar dendrites in the melt pool, while low G/R ratio favors the formation of a broad region of constitutional undercooling, resulting in the generation of equiaxed crystals [53]. For the dual-electron beam pattern, the reduced temperature gradient can effectively suppress columnar crystal growth [52,54].

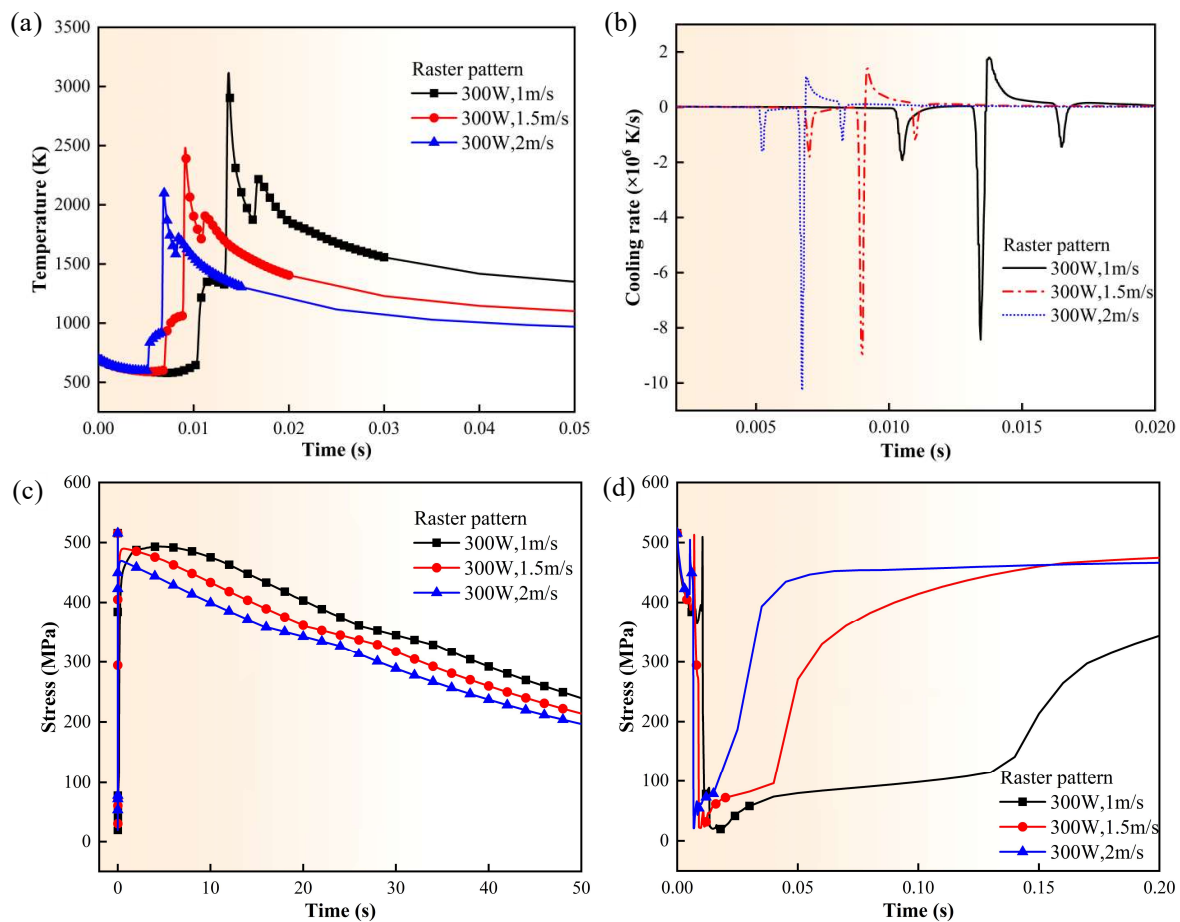


Figure 13. Time-dependent curve of temperature (a), cooling rate (b), and stress histories (c,d) under different scanning speed for raster pattern scanning path.

The temperature and stress histories under different power for dual-electron pattern are represented in Figure 15. From the temperature and cooling rate curve, it can be seen that point A experiences a significant temperature platform before reaching its peak temperature. The first temperature rise at point A is due to the thermal influence of the upper electron beam scanning track 6 on track 5, which can be demonstrated by the distance between the peaks of the cooling rate. Meanwhile, due to the temperature field influenced

by the interaction between two electron beams, the stress state during the melting process exhibits obvious differences from that of a single electron beam. There is clear phased downward trend. Comparing Figure 15d with Figure 11d, the trend of stress decrease during the solidification process is similar, indicating that changing only scanning strategy without changing the processing parameters will not change the stress evolution during the solidification process. Therefore, adopting a multi electron beam scanning strategy can reduce the temperature gradient of the melt pool without affecting residual stress through the mutual influence between each electron beam, thereby suppressing the formation of columnar crystals and producing more equiaxed crystals. This can reduce the anisotropy of material mechanical properties and improve forming efficiency [54,55].

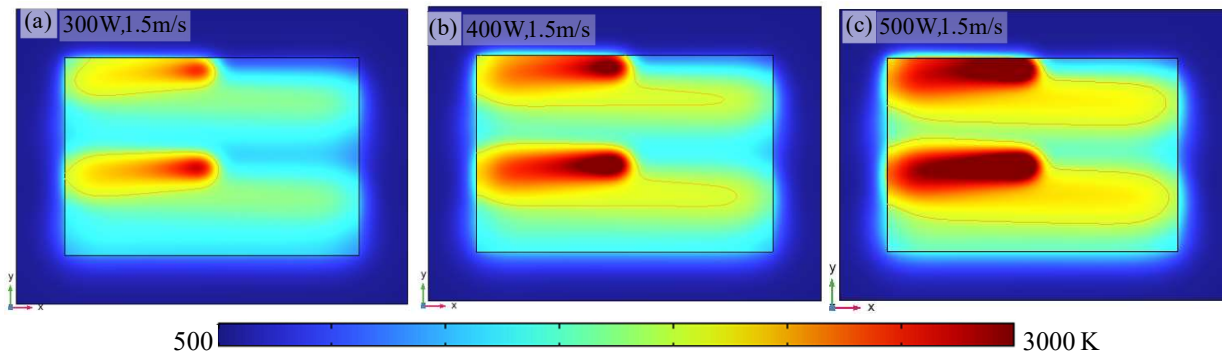


Figure 14. The temperature distribution under different power of (a) 300 W, (b) 400 W, and (c) 2 W at scanning speed of 1.5 m/s for dual-electron beam pattern.

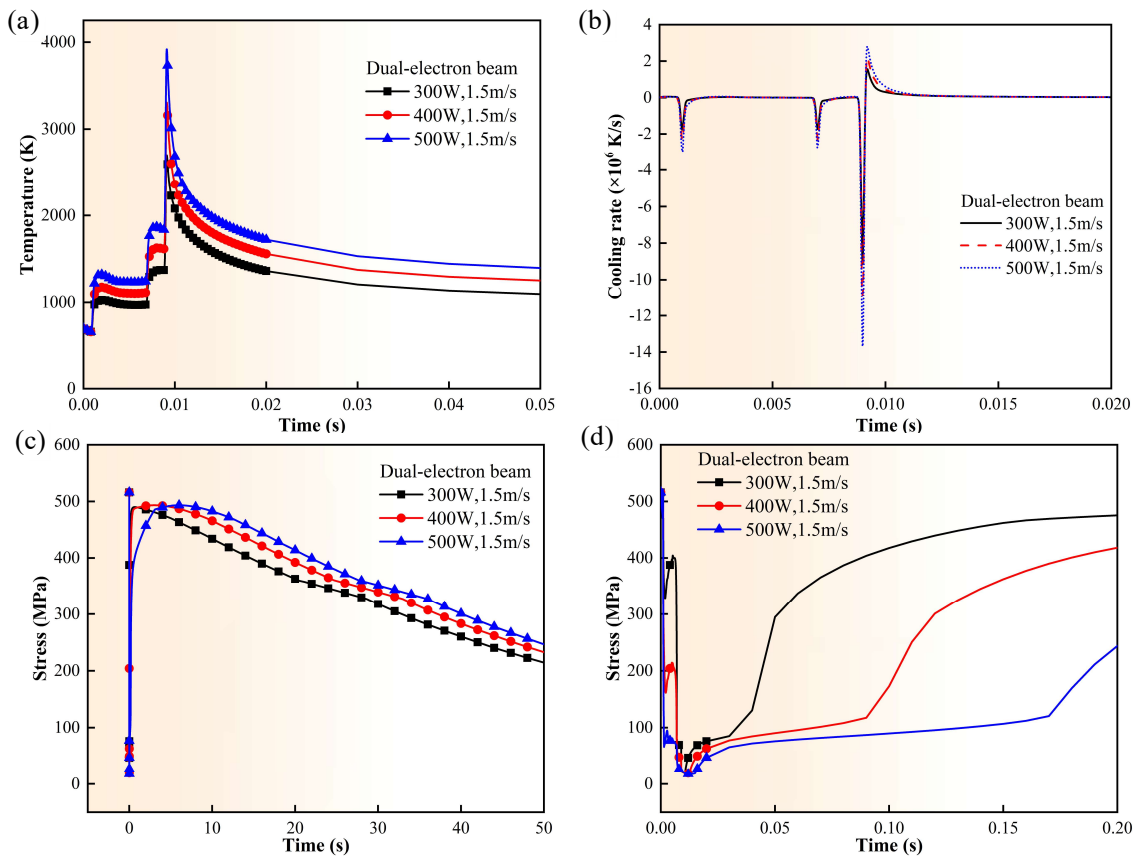


Figure 15. Time-dependent curve of temperature (a), cooling rate (b), and stress histories (c,d) under different power for dual-electron beam scanning strategy.

4. Conclusions

In current work, a FEM is established to investigate the temperature distribution and residual stress evolution of Ti6Al4V during the SEBM process. The single-layer and multi-channel scanning processes are simulation using a single electron beam as heat source. The results indicate that during the SEBM process, the thermal effects of adjacent trajectories are coupled in the melt pool, resulting in complex fluctuations in the temperature history curve. The melt pool exhibits obvious preheating, melting, and remelting phenomena. The stress in the molten pool during the solidification process rapidly increases in stages and then steadily decreases in the later stage, reflecting the thermal expansion and contraction process of the molten pool, which is a key factor affecting the formation of microstructures. In addition, by adjusting the scanning speed and electron beam energy, it was found that compared to electron beam energy, the adjustment of scanning speed has a more significant impact on temperature and stress. At the same time, the scanning paths of zigzag pattern and raster pattern are compared, and the results showed that the temperature distribution is more stable for the zigzag scanning pattern. Meanwhile, single layer and multi-channel scanning processes with dual-electron beam as heat source are investigated. Due to the temperature field of mutual influence between the two electron beams, the smaller temperature gradient of the melt pool compared to a single electron beam helps to suppress the growth of columnar crystals. For different scanning strategies, an electron beam energy of 300 W and a scanning speed of 1.5 m/s are considered as optimization parameters to avoid prolonged high-temperature stages induced by high electron beam energy and low scanning speed. These parameters are expected to suppress the formation of columnar β crystals and promote the development of more uniform grains in AM Ti alloys, while simultaneously achieving relatively low residual stress. Therefore, the current work is helpful in providing guidance on the selection of processing parameters and scanning strategies for SEBM.

Author Contributions: Q.F.: Conceptualization, Validation, Writing—review & editing, Supervision, Funding acquisition. P.Z.: Investigation, Data curation, Writing—original draft. J.L.: Conceptualization, Writing—review & editing, Supervision, Funding acquisition. H.W.: Supervision, Writing—review & editing, Funding acquisition. J.P.: Formal analysis, Software, Investigation, Data curation, Writing—original draft. All authors have read and agreed to the published version of the manuscript.

Funding: The authors would like to deeply appreciate the supports from National Natural Science Foundation of China (U2267252, 12372069, and 12172123), Yuelushan Center for Industrial Innovation (No. 2024YCH0106).

Data Availability Statement: The original contributions presented in this study are included in the article. Further inquiries can be directed to the corresponding author.

Conflicts of Interest: Author Pei Zhao was employed by Xi'an Sailong AM Technologies Co., Ltd. The remaining authors declare that the research was conducted in the absence of any commercial or financial relationships that could be construed as a potential conflict of interest.

References

1. Kürnsteiner, P.; Wilms, M.B.; Weisheit, A.; Gault, B.; Jäggle, E.A.; Raabe, D. High-strength Damascus steel by additive manufacturing. *Nature* **2020**, *582*, 515–519. [[CrossRef](#)] [[PubMed](#)]
2. Gu, D.; Shi, X.; Poprawe, R.; Bourell, D.L.; Setchi, R.; Zhu, J. Material-structure-performance integrated laser-metal additive manufacturing. *Science* **2021**, *372*, eabg1487. [[CrossRef](#)] [[PubMed](#)]
3. Ren, J.; Zhang, Y.; Zhao, D.; Chen, Y.; Guan, S.; Liu, Y.; Chen, W. Strong yet ductile nanolamellar high-entropy alloys by additive manufacturing. *Nature* **2022**, *608*, 62–68. [[CrossRef](#)]

4. Yue, H.; Peng, H.; Li, R.; Qi, K.; Zhang, L.; Lin, J.; Su, Y. Effect of heat treatment on the microstructure and anisotropy of tensile properties of TiAl alloy produced via selective electron beam melting. *Mater. Sci. Eng. A* **2021**, *803*, 140473. [[CrossRef](#)]
5. Körner, C. Additive manufacturing of metallic components by selective electron beam melting—A review. *Int. Mater. Rev.* **2016**, *61*, 361–377. [[CrossRef](#)]
6. Li, Y.; Liang, X.; Yu, Y.; Li, H.; Kan, W.; Lin, F. Microstructures and mechanical properties evolution of IN939 alloy during electron beam selective melting process. *J. Alloys Compd.* **2021**, *883*, 160934. [[CrossRef](#)]
7. Zhang, M.; Zhou, X.; Wang, D.; He, L.; Ye, X.; Zhang, W. Additive manufacturing of in-situ strengthened dual-phase AlCoCuFeNi high-entropy alloy by selective electron beam melting. *J. Alloys Compd.* **2022**, *893*, 162259. [[CrossRef](#)]
8. Li, Y.; Kan, W.; Zhang, Y.; Li, M.; Liang, X.; Yu, Y.; Lin, F. Microstructure, mechanical properties and strengthening mechanisms of IN738LC alloy produced by Electron Beam Selective Melting. *Addit. Manuf.* **2021**, *47*, 102371. [[CrossRef](#)]
9. Xiao, B.; Jia, W.; Tang, H.; Wang, J.; Zhou, L. Microstructure and mechanical properties of WMoTaNbTi refractory high-entropy alloys fabricated by selective electron beam melting. *J. Mater. Sci. Technol.* **2022**, *108*, 54–63. [[CrossRef](#)]
10. Kenevisi, M.S.; Lin, F. Selective electron beam melting of high strength Al2024 alloy; microstructural characterization and mechanical properties. *J. Alloys Compd.* **2020**, *843*, 155866. [[CrossRef](#)]
11. Wang, C.; Tan, X.; Liu, E.; Tor, S.B. Process parameter optimization and mechanical properties for additively manufactured stainless steel 316L parts by selective electron beam melting. *Mater. Des.* **2018**, *147*, 157–166. [[CrossRef](#)]
12. Teixeira, Ó.; Silva, F.J.; Ferreira, L.P.; Atzeni, E. A review of heat treatments on improving the quality and residual stresses of the Ti-6Al-4V parts produced by additive manufacturing. *Metals* **2020**, *10*, 1006. [[CrossRef](#)]
13. Biffi, C.A.; Fiocchi, J.; Ferrario, E.; Fornaci, A.; Riccio, M.; Romeo, M.; Tuissi, A. Effects of the scanning strategy on the microstructure and mechanical properties of a TiAl6V4 alloy produced by electron beam additive manufacturing. *Int. J. Adv. Manuf. Technol.* **2020**, *107*, 4913–4924. [[CrossRef](#)]
14. Yan, W.; Qian, Y.; Ge, W.; Lin, S.; Liu, W.K.; Lin, F.; Wagner, G.J. Meso-scale modeling of multiple-layer fabrication process in selective electron beam melting: Inter-layer/track voids formation. *Mater. Des.* **2018**, *141*, 210–219. [[CrossRef](#)]
15. Zhang, W.; Wang, H.; Kooi, B.J.; Pei, Y. Additive manufacturing of interstitial-strengthened high entropy alloy: Scanning strategy dependent anisotropic mechanical properties. *Mater. Sci. Eng. A* **2023**, *872*, 144978. [[CrossRef](#)]
16. Zhang, K.; Geng, J.; Liu, W.; Wang, W.; Wang, H.; Jiang, X.; Bian, H. Influences of scanning strategy on the quality, accuracy, microstructure and performance of Inconel 625 parts by LAM. *J. Mater. Res. Technol.* **2023**, *26*, 1962–1983. [[CrossRef](#)]
17. Sun, L.; Ren, X.; He, J.; Zhang, Z. Numerical investigation of a novel pattern for reducing residual stress in metal additive manufacturing. *J. Mater. Sci. Technol.* **2021**, *67*, 11–22. [[CrossRef](#)]
18. He, X.; Li, Y.; Bi, Y.; Liu, X.; Zhou, B.; Zhang, S.; Li, S. Finite element analysis of temperature and residual stress profiles of porous cubic Ti-6Al-4V titanium alloy by electron beam melting. *J. Mater. Sci. Technol.* **2020**, *44*, 191–200. [[CrossRef](#)]
19. Tunay, M.; Baykasoğlu, C.; Akyildiz, O.C.; To, A. A fully coupled thermal-microstructural-mechanical finite element process model for directed energy deposition additive manufacturing of Ti-6Al-4V. *Sci. Technol. Weld. Join.* **2023**, *28*, 118–127. [[CrossRef](#)]
20. Mishra, A.K.; Aggarwal, A.; Kumar, A.; Sinha, N. Identification of a suitable volumetric heat source for modelling of selective laser melting of Ti6Al4V powder using numerical and experimental validation approach. *Int. J. Adv. Manuf. Technol.* **2018**, *99*, 2257–2270. [[CrossRef](#)]
21. Liu, Z.; He, B.; Lyu, T.; Zou, Y. A review on additive manufacturing of titanium alloys for aerospace applications: Directed energy deposition and beyond Ti-6Al-4V. *JOM* **2021**, *73*, 1804–1818. [[CrossRef](#)]
22. Zhu, Y.; Zhang, K.; Meng, Z.; Zhang, K.; Hodgson, P.; Birbilis, N.; Huang, A. Ultrastrong nanotwinned titanium alloys through additive manufacturing. *Nat. Mater.* **2022**, *21*, 1258–1262. [[CrossRef](#)] [[PubMed](#)]
23. Zeng, Q.; Fu, G.; Peng, Q.; Xiao, H.; Li, S.; Zhang, Z. Numerical analysis of the effect of the spatial and temporal scanning strategies on the residual stress in the multi-laser powder bed fusion of Ti-6Al-4V. *Addit. Manuf.* **2024**, *88*, 104242. [[CrossRef](#)]
24. Riedlbauer, D.; Scharowsky, T.; Singer, R.F.; Steinmann, P.; Körner, C.; Mergheim, J. Macroscopic simulation and experimental measurement of melt pool characteristics in selective electron beam melting of Ti-6Al-4V. *Int. J. Adv. Manuf. Technol.* **2017**, *88*, 1309–1317. [[CrossRef](#)]
25. Maizza, G.; Caporale, A.; Polley, C.; Seitz, H. Micro-macro relationship between microstructure, porosity, mechanical properties, and build mode parameters of a selective-electron-beam-melted Ti-6Al-4V alloy. *Metals* **2019**, *9*, 786. [[CrossRef](#)]
26. Saboori, A.; Abdi, A.; Fatemi, S.A.; Marchese, G.; Biamino, S.; Mirzadeh, H. Hot deformation behavior and flow stress modeling of Ti-6Al-4V alloy produced via electron beam melting additive manufacturing technology in single β -phase field. *Mater. Sci. Eng. A* **2020**, *792*, 139822. [[CrossRef](#)]
27. Xu, W.; Brandt, M.; Sun, S.; Elambasseril, J.; Liu, Q.; Latham, K.; Qian, M. Additive manufacturing of strong and ductile Ti-6Al-4V by selective laser melting via in situ martensite decomposition. *Acta Mater.* **2015**, *85*, 74–84. [[CrossRef](#)]

28. Salsi, E.; Chiumenti, M.; Cervera, M. Modeling of microstructure evolution of Ti6Al4V for additive manufacturing. *Metals* **2018**, *8*, 633. [[CrossRef](#)]
29. Peng, J.; Liu, B.; Li, W.; Liaw, P.K.; Li, J.; Fang, Q. Data-driven investigation of microstructure and surface integrity in additively manufactured multi-principal-element alloys. *J. Alloys Compd.* **2023**, *937*, 168431. [[CrossRef](#)]
30. Le, T.N.; Lo, Y.L.; Tran, H.C. Multi-scale modeling of selective electron beam melting of Ti6Al4V titanium alloy. *Int. J. Adv. Manuf. Technol.* **2019**, *105*, 545–563. [[CrossRef](#)]
31. Michaleris, P. Modeling metal deposition in heat transfer analyses of additive manufacturing processes. *Finite Elem. Anal. Des.* **2014**, *86*, 51–60. [[CrossRef](#)]
32. Fernandez-Zelaia, P.; Kirka, M.M.; Rossy, A.M.; Lee, Y.; Dryepondt, S.N. Nickel-based superalloy single crystals fabricated via electron beam melting. *Acta Mater.* **2021**, *216*, 117133. [[CrossRef](#)]
33. Xiao, Z.; Chen, C.; Zhu, H.; Hu, Z.; Nagarajan, B.; Guo, L.; Zeng, X. Study of residual stress in selective laser melting of Ti6Al4V. *Mater. Des.* **2020**, *193*, 108846. [[CrossRef](#)]
34. Irwin, J.; Michaleris, P. A line heat input model for additive manufacturing. *J. Manuf. Sci. Eng.* **2016**, *138*, 111004. [[CrossRef](#)]
35. Chen, C.; Yin, J.; Zhu, H.; Xiao, Z.; Zhang, L.; Zeng, X. Effect of overlap rate and pattern on residual stress in selective laser melting. *Int. J. Mach. Tool. Manuf.* **2019**, *145*, 103433. [[CrossRef](#)]
36. Cheng, B.; Price, S.; Lydon, J.; Cooper, K.; Chou, K. On process temperature in powder-bed electron beam additive manufacturing: Model development and validation. *J. Manuf. Sci. Eng.* **2014**, *136*, 061018. [[CrossRef](#)]
37. Chaithanya Kumar, K.N.; Sharma, S.; Radhakrishnan, M.; Randhavan, R.; Verma, K.K.; Dowden, S.; Dahotre, N.B. Electron Beam Additive Manufacturing of SS316L with a Stochastic Scan Strategy: Microstructure, Texture Evolution, and Mechanical Properties. *Metals* **2024**, *14*, 1278. [[CrossRef](#)]
38. Maurya, A.K.; Yeom, J.T.; Kim, J.H.; Park, C.H.; Hong, J.K.; Yang, J.; Cho, S.M. Wire arc additive manufacturing method for Ti-6Al-4V alloy to improve the grain refinement efficiency and mechanical properties. *J. Mater. Res. Technol.* **2024**, *31*, 3003–3013. [[CrossRef](#)]
39. Liu, Z.; Zhao, D.; Wang, P.; Yan, M.; Yang, C.; Chen, Z.; Lu, Z. Additive manufacturing of metals: Microstructure evolution and multistage control. *J. Mater. Sci. Technol.* **2022**, *100*, 224–236. [[CrossRef](#)]
40. Liu, J.; Song, Y.; Chen, C.; Wang, X.; Li, H.; Wang, J.; Sun, J. Effect of scanning speed on the microstructure and mechanical behavior of 316L stainless steel fabricated by selective laser melting. *Mater. Des.* **2020**, *186*, 108355. [[CrossRef](#)]
41. Chen, H.; Fang, Q.; Zhou, K.; Liu, Y.; Li, J. Unraveling atomic-scale crystallization and microstructural evolution of a selective laser melted FeCrNi medium-entropy alloy. *CrystEngComm* **2020**, *22*, 4136–4146. [[CrossRef](#)]
42. Soylemez, E. High deposition rate approach of selective laser melting through defocused single bead experiments and thermal finite element analysis for Ti-6Al-4V. *Addit. Manuf.* **2020**, *31*, 100984. [[CrossRef](#)]
43. Wang, F.; Williams, S.; Colegrove, P.; Antonysamy, A.A. Microstructure and mechanical properties of wire and arc additive manufactured Ti-6Al-4V. *Metall. Mater. Trans. A* **2013**, *44*, 968–977. [[CrossRef](#)]
44. Cui, X.; Zhang, S.; Zhang, C.H.; Chen, J.; Zhang, J.B.; Dong, S.Y. Additive manufacturing of 24CrNiMo low alloy steel by selective laser melting: Influence of volumetric energy density on densification, microstructure and hardness. *Mater. Sci. Eng. A* **2021**, *809*, 140957. [[CrossRef](#)]
45. Bertsch, K.M.; De Bellefon, G.M.; Kuehl, B.; Thoma, D.J. Origin of dislocation structures in an additively manufactured austenitic stainless steel 316L. *Acta Mater.* **2020**, *199*, 19–33. [[CrossRef](#)]
46. Hu, D.; Grilli, N.; Yan, W. Dislocation structures formation induced by thermal stress in additive manufacturing: Multiscale crystal plasticity modeling of dislocation transport. *J. Mech. Phys. Solids* **2023**, *173*, 105235. [[CrossRef](#)]
47. Ali, M.H.; Han, Y.S. A Finite element analysis on the effect of scanning pattern and energy on residual stress and deformation in wire arc additive manufacturing of EH36 steel. *Materials* **2023**, *16*, 4698. [[CrossRef](#)]
48. Sun, L.; Ren, X.; He, J.; Zhang, Z. A bead sequence-driven deposition pattern evaluation criterion for lowering residual stresses in additive manufacturing. *Addit. Manuf.* **2021**, *48*, 102424. [[CrossRef](#)]
49. Sanchez, S.; Hyde, C.J.; Ashcroft, I.A.; Ravi, G.A.; Clare, A.T. Multi-laser scan strategies for enhancing creep performance in LPBF. *Addit. Manuf.* **2021**, *41*, 101948. [[CrossRef](#)]
50. Pfalz, T.; Rota, A.; Saeidnezhad, N.; Leyens, C. Comparison of different multi-laser powder bed fusion exposure strategies and their influence on the part quality of IN718. *Int. J. Adv. Manuf. Technol.* **2023**, *128*, 4469–4490. [[CrossRef](#)]
51. Peng, J.; Li, J.; Liu, B.; Wang, J.; Chen, H.; Feng, H.; Fang, Q. Formation process and mechanical properties in selective laser melted multi-principal-element alloys. *J. Mater. Sci. Technol.* **2023**, *133*, 12–22. [[CrossRef](#)]
52. Peng, J.; Li, J.; Liu, B.; Fang, Q.; Liaw, P.K. Origin of thermal deformation induced crystallization and microstructure formation in additive manufactured FCC, BCC, HCP metals and its alloys. *Int. J. Plast.* **2024**, *172*, 103831. [[CrossRef](#)]
53. Nie, P.; Ojo, O.A.; Li, Z. Numerical modeling of microstructure evolution during laser additive manufacturing of a nickel-based superalloy. *Acta Mater.* **2014**, *77*, 85–95. [[CrossRef](#)]

54. Zou, S.; Xiao, H.; Ye, F.; Li, Z.; Tang, W.; Zhu, F.; Zhu, C. Numerical analysis of the effect of the scan strategy on the residual stress in the multi-laser selective laser melting. *Results Phys.* **2020**, *16*, 103005. [[CrossRef](#)]
55. He, C.; Ramani, K.S.; Okwudire, C.E. An intelligent scanning strategy (SmartScan) for improved part quality in multi-laser PBF additive manufacturing. *Addit. Manuf.* **2023**, *64*, 103427. [[CrossRef](#)]

Disclaimer/Publisher's Note: The statements, opinions and data contained in all publications are solely those of the individual author(s) and contributor(s) and not of MDPI and/or the editor(s). MDPI and/or the editor(s) disclaim responsibility for any injury to people or property resulting from any ideas, methods, instructions or products referred to in the content.